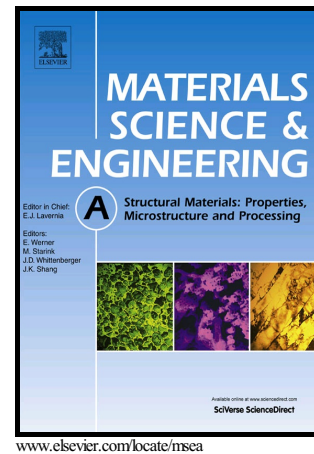


# Author's Accepted Manuscript

Controlling the high temperature mechanical behavior of Al alloys by precipitation and severe straining

C.M. Cepeda-Jiménez, M. Castillo-Rodríguez, J.M. Molina-Aldareguia, Y. Huang, T.G. Langdon, M.T. Pérez-Prado



PII: S0921-5093(16)31234-5  
DOI: <http://dx.doi.org/10.1016/j.msea.2016.10.026>  
Reference: MSA34228

To appear in: *Materials Science & Engineering A*

Received date: 21 September 2016  
Revised date: 5 October 2016  
Accepted date: 7 October 2016

Cite this article as: C.M. Cepeda-Jiménez, M. Castillo-Rodríguez, J.M. Molina Aldareguia, Y. Huang, T.G. Langdon and M.T. Pérez-Prado, Controlling the high temperature mechanical behavior of Al alloys by precipitation and severe straining, *Materials Science & Engineering A* <http://dx.doi.org/10.1016/j.msea.2016.10.026>

This is a PDF file of an unedited manuscript that has been accepted for publication. As a service to our customers we are providing this early version of the manuscript. The manuscript will undergo copyediting, typesetting, and review of the resulting galley proof before it is published in its final citable form. Please note that during the production process errors may be discovered which could affect the content, and all legal disclaimers that apply to the journal pertain

**Controlling the high temperature mechanical behavior of Al alloys by  
precipitation and severe straining**

C.M. Cepeda-Jiménez<sup>a\*</sup>, M. Castillo-Rodríguez<sup>a</sup>, J.M. Molina-Aldareguia<sup>a</sup>, Y. Huang<sup>b</sup>,  
T.G. Langdon<sup>b</sup>, M.T. Pérez-Prado<sup>a</sup>

<sup>a</sup>IMDEA Materials Institute, C/ Eric Kandel, 2, 28906 Getafe, Madrid, Spain

<sup>b</sup>Materials Research Group, Faculty of Engineering and the Environment, University of Southampton,  
Southampton SO17 1BJ, UK

\*Corresponding author.

**Abstract**

The aim of this work was to investigate the influence of the precipitate distribution on the microstructure and on the room and high temperature mechanical properties of an age-hardenable aluminium AA6082 alloy following severe straining by high-pressure torsion (HPT). With this goal, specimens in the as-cast and T6 peak-aged conditions were processed by HPT using 0.5, 1 and 5 turns at room temperature. At high strain levels ( $\gamma > 100$ ), similar saturation grain sizes ( $\sim 250$  nm), high-angle boundary fractions ( $\sim 80\%$ ) and hardness values ( $H_v \sim 160$ ) were obtained for both initial conditions. Grain refinement led to significant strengthening and to good ductility values at room temperature. Analysis by TEM and EDS elemental mapping revealed that HPT processing of the as-cast condition led to fracture of the stable  $\beta$ -phase into many small precipitates located preferentially along grain boundaries and triple junctions. By contrast, HPT processing of the T6 peak-aged specimens revealed a partial dissolution of the needle-shaped nanoprecipitates. The different evolutions of the precipitate distributions following straining in the as-cast and peak-aged conditions gave rise to dramatic differences in the mechanical properties and the operative deformation mechanisms at warm temperatures. These results provide evidence that the high temperature mechanical behavior of age-hardenable Al alloys may be conveniently controlled by altering the precipitate distribution followed by severe straining.

**Keywords**

Al-Mg-Si alloy; High pressure torsion; Precipitates; Deformation mechanisms;  
Microstructure

## 1. Introduction

Al-Mg-Si alloys are widely used for demanding structural applications due to their good physical and chemical properties [1-3]. The alloy with the designation AA6082 is optimized to be the strongest alloy in the family. Good formability, low density and good weldability, together with low cost, are factors making this alloy commercially very attractive.

The mechanical properties of the AA6082 alloy are typically optimized by artificial aging. Al-Mg-Si alloys present a complex precipitation sequence which is generally accepted to be: (a) aluminum supersaturated solid solution (SSS), (b) clusters of Si and Mg atoms (GP-I and GP-II) zones, (c) metastable  $\beta''$  needle-shape precipitates with a monoclinic structure, (d) metastable  $\beta'$  rod-like precipitates with a hexagonal crystal structure, and (e) stable  $\beta$  phase, which is usually  $\text{Mg}_2\text{Si}$  platelets having the cubic  $\text{CaF}_2$  structure [4-7]. The metastable  $\beta''$  phase has been observed as the dominant phase present at the peak-aging condition where maximum hardness occurs [5,6]. Processing parameters such as the temperature and time during heat treatments or the level of strain during hot or cold working are also reported to influence the mechanical properties of these alloys [8-10].

Severe plastic deformation (SPD) processes have been extensively utilized for grain refinement of Al alloys down to the submicrometer or nanometer levels and this has led to the development of microstructures with very high strength which is consistent with the Hall-Petch relationship [11,12]. Among all SPD techniques, high-pressure torsion (HPT) is the method producing the smallest grain sizes and the highest fraction of high-angle grain boundaries [13]. A detailed description of the principles of HPT is given in earlier reports [14]. In age-hardenable alloys, SPD processes may additionally be utilized to tailor the precipitate distribution. Simultaneously, the high strains involved

lead naturally to a high density of defects whose interactions with precipitates and solutes lead to even higher strengthening levels. For example, a yield strength of 1 GPa was achieved in an Al-Zn-Mg-Cu alloy processed by HPT [15]. Furthermore, it has been extensively reported [11,16-18] that, since precipitates may contribute to greatly enhance the stability of the ultrafine-grained structures at high temperatures, SPD-processed age-hardenable alloys are often capable of exhibiting superplastic properties when tested in tension after processing [17].

For Al-Mg-Si alloys, most research related to SPD has been carried out in the solid solution state. More specifically, several earlier reports investigated the capability of HPT processing of solid solution Al-Mg-Si alloys to stimulate solute segregation to grain boundaries (GBs) [10,19-22]. However, a comparatively smaller number of works have dealt with age-hardened Al-Mg-Si alloys. In particular, although a few studies have exploited SPD techniques such as equal-channel angular pressing (ECAP) to fragment or even dissolve pre-existing precipitates [2,23,24], the effect of HPT processing on the microstructural development, including the precipitate distribution, and the mechanical behavior at room and high temperatures of age-hardened Al-Mg-Si alloys remains essentially unknown [20].

The aim of the present work is to analyze the microstructural evolution and the mechanical behavior at room and warm temperatures of an HPT-processed AA6082 alloy. More specifically, HPT was carried out on the alloy at room temperature in two initial conditions, namely as-cast and T6 peak-aged, in order to compare the effect of the original precipitate morphology and distribution on the severely strained microstructures, as well as on the mechanical properties and deformation mechanisms at room temperature and at 250°C. The microstructure of the AA6082 alloy was carefully analyzed by electron back-scattered diffraction (EBSD) and transmission electron

microscopy (TEM) before and after HPT processing. The mechanical behavior was characterized by hardness and tensile tests. This work provides a background for the development of thermally-stable ultrafine-grained aluminium alloys containing second-phase particles.

## 2. Experimental procedure

The material employed in this work is a commercial AA6082 aluminium alloy. The starting material was a 4 cm thickness plate in the as-cast condition with a composition of Al- 0.67 wt.%Si-0.19 wt.%Mn- 0.52 wt.%Mg-0.01 wt.% Cr-0.02 wt.%Fe- 0.02 wt.% Zn- 0.06 wt.% Ti. During casting, the alloy was mechanical stirred for 2 min at 780°C using an impeller and then it was ultrasonicated (17.5kHz, 35  $\mu$ m amplitude) at 720 °C for 10 min and cast at 710 °C in a metallic mold. It is important to note that this alloy does not contain elements such as zirconium or scandium which are commonly added to produce nanoscale dispersoids acting as effective pinning agents to hinder the migration of grain boundaries at high temperatures [25,26].

Two separate sets of disk samples, with dimensions ~1 mm in thickness and 10 mm in diameter, were machined for HPT processing. The first set was kept in the as-cast condition and the second set was subjected to a T6 heat treatment which involves solution treating at 530 °C for 1 h followed by rapid quenching in water and finally age hardening at 180 °C for 6 h. This treatment gives rise to a very fine dispersion of hardening nanoprecipitates inside the grains. Henceforth, these two initial states are designated as the as-cast and T6 peak-aged conditions. The two sets of samples were then subjected to HPT processing at room temperature using a quasi-constrained HPT facility where lateral flow of the material is only partially restricted. The imposed pressure was maintained constant during processing at 6 GPa and separate disks were

processed using 0.5, 1 and 5 turns at a fixed rotational speed of 1 rpm. The final thickness of the HPT samples was ~0.8 mm.

The microstructures before and after HPT processing were examined by EBSD and TEM. The EBSD microtexture measurements were carried out using a Helios NanoLab 600i FEI field emission gun scanning electron microscope (FEG-SEM) equipped with a NordlysMax detector, a CCD camera, the AZtekHKL data acquisition software and the Channel 5.0 post-processing analysis package. The FEG-SEM operating conditions were an accelerating voltage of 15 kV and a current intensity of 2.7 nA with a step size of ~1.7  $\mu\text{m}$  and 0.015  $\mu\text{m}$  for the as-received materials and HPT-processed samples, respectively. Average grain size values ( $d$ ) were calculated by the linear intercept method from inverse pole figure maps (IPF) in the normal direction (ND) to the surface of the HPT disks at different positions along the radius, considering only GBs with misorientation angles greater than 15°. Sample preparation for EBSD included mechanical mirror-polishing using diamond pastes of increasingly finer particle sizes and a colloidal silica slurry finishing.

In addition, the microstructure of the as-cast and SPD-processed samples was also examined by TEM using a Talos F200X FEI operating at 200 kV. Characterization was performed both in conventional transmission with a parallel beam as well as in scanning transmission electron microscopy (STEM) mode using high angle annular dark field (HAADF) imaging with a probe size of 0.2 nm and a convergence angle of 34 mrad. Elemental mapping was also carried out using energy dispersive X-ray spectroscopy (EDS) in order to investigate the distribution of precipitates and alloying elements before and after HPT processing. Samples were ground mechanically and then polished to perforation using a twin-jet electropolishing system with a solution of 30% nitric acid in methanol at -28 °C and 15 V.

The mechanical behaviour of the as-received and processed samples was characterized by hardness and tensile testing. The Vickers microhardness was measured along two diameters on the HPT disk surfaces using a Shimadzu HMV-2 microhardness tester with a load of 0.5 kg and a dwell time for each separate measurement of 15 s. The distance from each indentation centre to the centre of the disk was measured using the Sigma Scan Pro image analysis software. Dog-bone tensile samples with 10 mm gage length and transversal sections of  $3 \times 1.5 \text{ mm}^2$  were electro-discharge machined out of the two as-received materials (as-cast and T6 peak-aged). In addition, small tensile specimens were also electro-discharge machined from the HPT disks with 3 mm gage length and transversal sections of  $\sim 0.8 \times 1 \text{ mm}^2$ . Tensile tests were then carried out at room temperature (RT) and 250°C with an initial strain rate of  $10^{-3} \text{ s}^{-1}$  using a universal electromechanical testing machine INSTRON 3384. Two tests per sample were performed to failure with the aim of characterizing the full macro-mechanical response (yield and maximum strength and ductility). Finally, EBSD analysis was performed in the gage regions of some deformed samples in order to evaluate possible microstructural changes following testing.

### 3. Experimental results

#### 3.1. Initial microstructure, precipitate size and distribution.

Fig. 1 illustrates the microstructure and misorientation distribution histograms of the as-cast (Fig. 1a) and T6 peak-aged AA6082 alloy (Fig. 1b) having average grain sizes ( $d$ ) of 84 and 88  $\mu\text{m}$ , respectively. Both materials exhibit similarly weak microtextures with a high fraction of low-angle boundaries (Fig. 1c) due, in the case of the as-cast alloy, to the mechanical and ultrasonic cavitation stirring during casting and, for the T6 peak-aged material, to the rapid quenching following the solution treatment.

Fig. 2 shows bright field TEM images (Figs. 2a and b) corresponding to the as-cast condition. Only needle-shaped precipitates of approximately 500 nm in length, and their cross-sections, are observed along the selected [011] zone axis. The appearance of these precipitates corresponds to the stable  $\beta$  phase ( $\text{Mg}_2\text{Si}$ ), which was confirmed by EDS elemental maps (Figs. 2c-e). This phase is characteristic of over-aging treatments [4] and its presence in the as-cast condition is associated with the slow cooling rate after the casting process.

By contrast, the T6 peak-aged sample (Fig. 3) exhibits only nanoscale needle-shaped precipitates,  $\sim 10$  nm in length and  $\sim 4$  nm in diameter, which are homogeneously distributed in the aluminium matrix and are clearly seen as dark and white dots, respectively, on the bright field and STEM-HAADF images (Figs. 3a and b). The corresponding Mg and Si EDS maps are illustrated in Figs. 3c and d. The present results are consistent with earlier investigations which reported that the maximum strength is achieved at peak-aging due to a high density of needle-shape  $\beta''$  ( $\text{Mg}_5\text{Si}_6$ ) and  $\beta'$  ( $\text{Mg}_9\text{Si}_5$ ,  $\text{Mg}_6\text{Si}_3$ ) nanoprecipitates which are aligned along the three equivalent  $\langle 001 \rangle$  directions of the *fcc* Al matrix [6,7,10].

### 3.2. Microstructure evolution during HPT processing

Fig. 4 shows the EBSD IPF maps in the ND to the disk surface of the as-cast (Fig. 4a) and T6 peak-aged (Fig. 4b) AA6082 alloy processed by HPT using 0.5 anvil turns. Both maps were acquired at regions located to 0.2 mm from the centre of the disk where the equivalent shear strain ( $\gamma$ ) is approximately 0.63. This low level of strain produces a highly inhomogeneous structure populated with dislocation networks and cells, and mainly constituted by low-angle dislocation boundaries (Fig. 4c). Nevertheless, small grains are already present in the HPT-processed as-cast material (Fig. 4a) where the fraction of high-angle boundaries (HABs) ( $f_{\text{HABs}}$ ) amounts to approximately 40%. In the

T6 peak-aged alloy, on the contrary,  $f_{\text{HGAs}}$  is only about 12%. This difference is attributed to the presence of nanoprecipitates in the T6 peak-aged conditions which, in their capacity as dislocation pinning sites, favor the density of accumulated dislocations to reach a higher level than may be achieved for the as-cast material.

Fig. 5 illustrates the EBSD IPF maps in the ND to the disk surface of the as-cast (Fig. 5a) and T6 peak-aged (Fig. 5b) AA6082 alloy processed by HPT using 5 anvil turns. Both maps were acquired at regions located to 0.2 mm from the centers of the disks where the equivalent shear strain ( $\gamma$ ) is approximately 6.3. It is evident that, with increasing strain, the grain structure gradually becomes more homogeneous, the grain size decreases and  $f_{\text{HGAs}}$  increases (Fig. 5d). The  $d$  values corresponding to the as-cast and T6 peak-aged materials are, respectively, 786 nm and 350 nm (Fig. 5e). The finer grain size of the T6-treated condition is due to the presence of the nanoprecipitates. In aluminium-based alloys it is well known the introduction of very fine second-phase particles induces a high dislocation density during deformation and leads to faster structural refinement based on the formation of large strain and misorientation gradients in the matrix close to these particles [27,28]. It can be seen in Fig. 5 that the texture corresponding to the HPT-processed as-cast material remains relatively weak (Fig. 5a). An incipient development of the commonly observed shear texture components, i.e. A  $\{111\}\langle 110\rangle$ , B  $\{112\}\langle 110\rangle$  and C  $\{001\}\langle 110\rangle$ , which are schematically displayed in Fig. 5c, can be observed where  $\{hkl\}$  is parallel to the  $z$  direction (torsion axis) and  $\langle uvw\rangle$  is parallel to the shear direction ( $\theta$ ) which is tangential to the anvil rotation [29]. Fcc metals such as aluminium, with high stacking fault energy, present simple shear textures consisting of a strong  $\{hkl\}\langle 110\rangle$  B fibre and a less strong  $\{111\}\langle uvw\rangle$  A fibre [30] in the early stages of HPT processing. In aluminium, the ideal  $\{001\}\langle 110\rangle$  (C orientation) and  $\{112\}\langle 110\rangle$  (B orientation) components are normally positions of high

orientation density on the B fibre, due to the strong tendency for the slip direction to become aligned with the shear direction [31,32]. The T6 peak-aged condition (Fig. 5b) shows a pronounced C  $\{001\}\langle 110\rangle$  simple-shear texture component.

Additional further levels of straining lead to texture weakening, to enhanced grain refinement and, thus, to a higher fraction of HABs. Fig. 6 illustrates the EBSD IPF maps in the ND to the disk surface of the as-cast (Fig. 6a) and T6 peak-aged (Fig. 6b) AA6082 alloy processed by HPT using 5 anvil turns. Both maps were acquired at regions located close to the edge of the disks, where the equivalent shear strain ( $\gamma$ ) is approximately 141. It can be seen that the microstructure is reasonably homogeneous and that very fine and equiaxed grains are obtained for both conditions. The average  $d$  values were, respectively, 265 and 251 nm. Similar grain size saturation values were achieved in AA6061 alloy ( $\sim 250$  nm) [33] and Al-1wt% Mg alloy ( $\sim 230$  nm) [34] after 10 HPT revolutions. The increase in strain tends to decrease the texture strength down to approximately random levels and also shift the distribution of grain boundary misorientation angles towards higher values (Fig. 6c). The texture randomization is due to the fact that as the strain increases, some of the cell block, or cell band boundaries evolve to form higher misorientation boundaries, undergoing a rigid body rotation of adjacent crystallites, which leads to an increase in the orientation spread [32]. The initial precipitate distribution appears to have little influence on the deformed grain size when the samples are processed to high levels of strain, suggesting that the interparticle spacing is larger than the achieved grain size [2].

Fig. 7 gives further information on the distribution of precipitates at the edge of the HPT disk of the as-cast AA6082 alloy processed using 5 turns at room temperature. Consistently with Fig. 6a, the fine grain size and high misorientation levels give rise to almost continuous diffraction rings in the SAED pattern of Fig. 7a. The STEM

micrographs (Figs. 7b and c) and the EDS Mg and Si maps of Figs. 7d and e reveal that the rod-like precipitates present initially in the as-cast condition have been fragmented by shearing during HPT processing into many small precipitates having sizes ranging between ~5 and 25 nm (red arrows in Figs. 7b and c). Many of these nanoprecipitates appear to be located along GBs but others were observed at triple junctions.

Fig. 8 is formed by several TEM micrographs corresponding to the edge of the HPT disk of the T6 peak-aged AA6082 alloy processed using 5 turns at room temperature. No sign of the presence of nanoprecipitates at grain boundaries was detected by TEM, STEM or EDS analysis. Instead, the initial fine  $\beta''$  and  $\beta'$  needle-shaped precipitates appear to have been sheared and partially dissolved by deformation. GB segregation of Mg and Si, extensively reported in aluminium alloys subjected to SPD [10,20,21,35-37], cannot be ruled out since these solute-rich thin layers may only be accurately detected by atom probe analysis [10,15,37].

### 3.3. Hardness evolution of the HPT-processed AA6082 alloys

Fig. 9 illustrates the hardness distributions along two disk diameters corresponding to both initial conditions, as-cast (Fig. 9a) and T6 peak-aged (Fig. 9b), processed using 0.5, 1 and 5 anvil turns. The lower broken line included in both graphs shows the average hardness value corresponding to the unprocessed as-cast (Fig. 9a) and T6 peak-aged (Fig. 9b) conditions, respectively. The microhardness values are re-plotted in Fig. 9c against the shear equivalent strain ( $\gamma$ ), calculated using the equation  $\gamma=2\pi Nr/h$  where  $N$  is the number of HPT revolutions,  $r$  is the radial distance from the disk center and  $h$  is the thickness of the disk. The hardness of the processed as-cast material increases continuously with strain until a saturation value of approximately  $HV\approx 158$  is obtained at shear strains close to 100. However, the hardness of the T6 peak-aged material

reaches this same saturation value following the application of a shear strain as small as 15. The fact that both materials reach ultimately similar hardness levels at sufficiently severe strains suggests that ultimately the grain size is the main strengthening factor. The need for higher strains to reach the saturation level in the HPT-processed as-cast AA6082 alloy is consistent with the slower rate of grain refinement in this condition, together with the presence of comparatively larger precipitates up to high strain levels.

These results clearly demonstrate that, in addition to the strain imposed during the HPT processing, the initial precipitate distribution also plays a significant role in the kinetics of grain refinement, in strain hardening and in the evolution of precipitates during straining and thus on the final mechanical properties.

#### *3.4. Tensile properties of the AA6082 processed by HPT*

Typical plots of true stress versus true plastic strain are shown in Fig. 10 for both as-cast (Fig. 10a) and T6 peak-aged (Fig. 10b) materials processed by HPT through 0.5 and 5 turns and then tested at RT with an initial strain rate of  $10^{-3} \text{ s}^{-1}$ . Also included in Fig.10 are curves corresponding to the as-received unprocessed materials. The shear strains corresponding to the gage lengths of samples processed using 0.5 and 5 turns are  $\gamma \sim 5$  and  $\gamma \sim 50$ , respectively. It can be clearly seen that severe straining leads to significant increases of the RT yield strength, ultimate tensile stress and ductility. More specifically, the yield strength of the samples processed to shear strains of 50 increases four times in the as-cast material (Fig. 10a) and almost doubles in the T6 condition (Fig. 10b). The maximum yield strength attained ( $\sigma_{0.2} \sim 527 \text{ MPa}$ ), corresponding to the T6 condition at  $\gamma \sim 50$  (5 turns), is superior to that exhibited by high-strength Al-Zn-Mg-(Cu) alloys containing a large amount of alloying elements [38]. The overall higher stress levels of the T6 peak-aged sample at  $\gamma \sim 50$  are consistent with the faster grain refinement kinetics and the higher hardness measured at such strain levels (Fig. 9c). The

increase in ductility with straining is attributed to the fine grain sizes developed during HPT processing.

Fig. 11 illustrates the tensile true stress-true plastic strain response at 250°C and at an initial strain rate of  $10^{-3} \text{ s}^{-1}$  corresponding to the as-cast (Fig. 11a) and T6 peak-aged samples (Fig. 11b) before and after HPT processing using 0.5 and 5 turns. It can be appreciated that severe straining of the as-cast material (Fig. 11a) results in significant increases of the yield, ultimate tensile strength and ductility. However, on the contrary, the T6 peak-aged samples become softer, albeit more ductile, following HPT processing (Fig. 11b).

The notable differences in the high temperature mechanical behavior of the two materials investigated (Fig. 11) suggest that deformation is being controlled by different micromechanisms. In particular, it seems likely that the softening and the relatively large elongations observed in the T6 peak-aged samples may reflect a higher contribution of high temperature mechanisms such as grain boundary sliding (GBS). Occurrence of GBS during deformation leaves several footprints, which can be traced post-mortem by microstructural analysis of the tested specimens. The most important are texture weakening and the retention of equiaxed grain sizes [39]. In the present study, both materials exhibited very weak textures at the beginning of the test (Fig. 6) and, since the elongations to failure in both cases are relatively moderate, significant changes in the texture are not expected. However, the morphology of the grains should provide an indirect indicator of the dominant micromechanisms. Fig. 12 illustrates the microstructures of the as-cast (Fig. 12a) and T6 peak-aged (Fig. 12b) materials processed by HPT using 5 turns and then tested at 250°C until failure. The tensile direction is indicated by the horizontal arrow. As expected, the texture of both materials remains fairly random after straining. In the as-cast material (Fig. 12a) the average grain

size after tensile testing is approximately 660 nm, with visible grain elongation along the tensile axis. The final grain aspect ratio ( $d_l/d_t$ ) is 1.36, where  $d_l$  is the average grain size measured along the longitudinal direction (parallel to the tensile axis) and  $d_t$  is the average grain size measured along the transverse direction (perpendicular to the tensile axis). In the T6 peak-aged condition (Fig. 12b) the grain size increases more noticeably after tensile testing, reaching an average value of 1  $\mu\text{m}$ . Moreover, despite the relatively high elongations achieved, the grains remain fairly equiaxed with  $(d_l/d_t) \sim 1.12$ . The evolution of the microstructure during high temperature tensile testing suggests that, while in the as-cast material dislocation slip appears to dominate the deformation, in the T6 peak-aged material GBS seems to play a more important role.

#### 4. Discussion

Among its many uses, high-pressure torsion is very effective in altering the precipitation state of alloys and, more importantly, that of age-hardenable Al alloys [13]. The present results are consistent with several aspects put forward in earlier research related to the effect of severe plastic deformation on the distribution of precipitates in Al alloys.

First, there is clear evidence that HPT is very efficient in breaking relatively large precipitates, such as those present in the as-cast Al6082 alloy, into much finer precipitates (Fig. 7), thereby contributing to dramatically enhancing the room temperature strength and thermal stability (Figs. 10,11). Previous studies [17,40] on an overaged Al-Mg-Si alloy severely deformed by ECAP showed that rods of  $\beta'$  phase with 100-200 nm length were broken into small fragments having lengths of several tens of nanometers and also possibly partially dissolved. Such small precipitates are very useful in enhancing the thermal stability of these severely strained microstructures.

Second, evidence is provided for the ability of HPT to dissolve nanoprecipitates, such as those present in the T6 peak-aged alloy. This observation is in agreement with previous studies in Al-Mg-Si alloys where the  $\beta''$  needles were shown to fully dissolve by severe plastic deformation [2,7]. Dissolution is commonly followed by grain boundary segregation. The presence of a supersaturated solid solution at GBs has been attributed to the constant flow of dislocations and vacancies as well as to the sweeping of alloying elements from the bulk by moving GBs [21,41].

Additionally, the current study demonstrates that the high temperature mechanical properties of the AA6082 alloy, and also the associated active deformation mechanisms, can be controlled by altering the initial precipitation and solute distribution followed by severe straining. In particular, the results show that the HPT-processed as-cast AA6082 alloy retains high temperature mechanical stability while the HPT-processed T6 peak-aged alloy softens with increasing temperature. The remarkably different high temperature mechanical behavior of the severely deformed as-cast and T6 peak-aged materials is related to their corresponding post-processing distribution of precipitates and solutes. In particular, the observed strengthening of the as-cast sample is probably due to the presence of very fine precipitates along the grain boundaries which may act as strong pinning points and thus prevent grain growth or boundary sliding. By contrast, the HPT-induced dissolution of the nanoprecipitates that were initially present in the T6 peak-aged specimen favors the activation of GBS [17,26] and this produces a higher ductility and lower flow stress that may be useful for forming processes. It was reported earlier that the occurrence of GBS in an ultrafine grained Al-Zn alloys after HPT processing is favored by the presence of a solute-rich layer along the GBs [42,43]. However, it was not possible to detect these segregations in the present research because

any estimation by analytical TEM of low levels of segregation was severely hindered due to the similar atomic numbers of Si, Mg and Al [10].

In summary, the main highlight of the paper is that it provides sound evidence that the high temperature mechanical behavior of the Al alloy investigated can be altered dramatically by tuning the precipitate distribution followed by severe straining. In particular, high pressure torsion (HPT) of the alloy in the as-cast and T6 peak aged conditions leads to variations in the ultimate tensile strength at 250°C of more than 100 MPa (increment of 100%) and, simultaneously, to 25% variations in the engineering strain. The origin of such dramatic differences in the high temperature behavior is attributed to the evolution of the precipitate distribution during severe straining by HPT. In particular, the relatively coarse particles present in the as-cast samples break into thermally stable nanoprecipitates that pin the grain boundaries, while the nanoprecipitates present in the T6 conditions tend to dissolve, thus allowing the onset of grain boundary sliding. The room temperature mechanical behavior is, however, little affected by the precipitate distribution and it is shown that the strength is mainly provided by the ultrafine grain size, which is similar for both conditions. HPT processing of Al alloys with nanoprecipitates has, thus, been found as a very useful tool to fabricate alloys with high strength and high ductility at high temperatures. It is anticipated that the same approach may be applied to optimize the high temperature properties of other two-phase metallic alloys.

## 5. Summary and conclusions

1. Room temperature HPT processing to very large strains leads to a stabilization, in both as-cast and T6 peak-aged AA6082 alloys, of an ultra-fine grained microstructure with an equiaxed average grain size of  $\sim 250$  nm and a  $f_{\text{HAB}} \sim 80\%$ .

The saturation grain sizes, close to 250 nm, appear to be independent of the initial condition. The rate of grain size refinement is higher in the T6 peak-aged condition.

2. HPT processing of the as-cast material to very large strains leads to fracture of the rod-like precipitates which are present initially in the alloy, thereby producing many nanoprecipitates located preferentially along GBs and triple junctions. HPT processing of the T6 peak-aged alloy to very large strains led to shearing and partial dissolution of the  $\beta''$  and  $\beta'$  needle-shaped nanoprecipitates.
3. The initial precipitate distribution appears to have little influence on the room temperature mechanical properties of the HPT processed AA6082 alloy. In both the as-cast and the T6 peak-aged condition, severe straining leads to significant increases in the yield strength, ultimate tensile strength and ductility. The grain size becomes the main strengthening mechanism, as is typically observed in metallic materials processed by severe plastic deformation methods. At RT the Vickers microhardness reached a saturation value in both the as-cast and T6 peak-aged alloys of  $\sim 160$  HV at  $\gamma \sim 100$ .
4. The initial precipitate distribution has a significant influence on the high temperature mechanical behavior of the HPT-processed AA6082 alloy. In particular, the presence of small precipitates along GBs in the HPT-processed as-cast material leads to higher strength levels than in the corresponding unprocessed samples, as dislocation slip, arrested by precipitate-stabilized grain boundaries, is the dominant deformation mechanism. However, in the HPT-processed T6 peak-aged alloy, where boundaries are more mobile due to the more homogeneous distribution of precipitates and solutes, grain boundary

sliding is observed to contribute to deformation leading to significant softening with respect to the corresponding unprocessed alloy.

5. These results demonstrate that the high temperature mechanical response of age-hardenable Al-Mg-Si alloys can be dramatically altered by heat treatments designed to generate different precipitate distributions followed by severe straining. Accordingly, this opens a new avenue for the development of Al alloys with tailored properties at high temperatures.

### **Acknowledgements**

The authors wish to acknowledge financial support from the European Commission (ExoMet Project, 7th Framework Programme, contract FP7-NMP3-LA-2012-280421) and the Spanish Ministry of Science and Competitiveness (project MAT2012-31889). The research leading to these results also received funding from Madrid region under programme S2013/MIT-2775, DIMMAT project. Two of the authors (YH and TGL) were supported by the European Research Council under ERC Grant Agreement No. 267464-SPDMETALS.

### **References**

1. C.D. Marioara, S.J. Andersen, J. Jansen, H.W. Zanbergen, Atomic model for GP-zones in a 6082 Al-Mg-Si system, *Acta Mater.* 49 (2001) 321-328.
2. I. Gutierrez-Urrutia, M.A. Muñoz-Morris, D.G. Morris, The effect of coarse second-phase particles and fine precipitates on microstructure refinement and mechanical properties of severely deformed Al alloy, *Mater. Sci. Eng. A* 394 (2005) 399-410.

3. S. Dadbakhsh, A. Karimi Taheri, C.W. Smith, Strengthening study on 6082 Al alloy after combination of aging treatment and ECAP process, *Mater. Sci. Eng. A527* (2010) 4758-4766.
4. M. Cabibbo, S. Spigarelli, E. Evangelista, A TEM investigation on the effect of semisolid forming on precipitation processes in an Al-Mg-Si alloy, *Mater. Charact.* 49 (2003) 193-202.
5. D.J. Chakrabarti, D.E. Laughlin, Phase relations and precipitation in Al-Mg-Si alloys with Cu additions, *Progress Mater. Sci.* 49 (2004) 389-410.
6. M.A. van Huis, J.H. Chen, H.W. Zandbergen, M.H.F. Sluiter, Phase stability and structural relations of nanometer-sized, matrix-embedded precipitate phases in Al-Mg-Si alloys in the late stages of evolution, *Acta Mater.* 54 (2006) 2945-2955.
7. H.J. Roven, M. Liu, J.C. Werenskiold, Dynamic precipitation during severe plastic deformation of an Al-Mg-Si aluminium alloy, *Mater. Sci. Eng. A* 483-484 (2008) 54-58.
8. G.K. Quainoo, S. Yannacopoulos, The effect of cold work on the precipitation kinetics of AA6111 aluminum, *J. Mater. Sci.* 39 (2004) 6495-6502.
9. R.S. Yassar, D.P. Field, H. Weiland, The effect of predeformation on the  $\beta''$  and  $\beta'$  precipitates and the role of Q' phase in an Al-Mg-Si alloy; AA6022, *Scripta Mater.* 53 (2005) 299-303.
10. X. Sauvage, E.V. Bobruk, M.Yu. Murashkin, Y. Nasedkina, N.A. Enikeev, R.Z. Valiev, Optimization of electrical conductivity and strength combination by structure design at the nanoscale in Al-Mg-Si alloys, *Acta Mater.* 98 (2015) 355-366.
11. S.V. Dobatkin, E.N. Bastarache, G. Sakai, T. Fujita, Z. Horita, T.G. Langdon, Grain refinement and superplastic flow in an aluminum alloy processed by high-pressure torsion, *Mater. Sci. Eng. A* 408 (2005) 141-146.

12. A. Deschamps, F. De Geuser, Z. Horita, S. Lee, G. Renou, Precipitation kinetics in a severely plastically deformed 7075 aluminium alloy, *Acta Mater.* 66 (2014) 105-117.
13. A.P. Zhilyaev, T.G. Langdon, Using high-pressure torsion for metal processing: Fundamentals and applications, *Prog. Mater. Sci.* 53 (2008) 893.
14. A.P. Zhilyaev, B.K. Kim, J.A. Szpunar, M.D. Baró, T.G. Langdon, The microstructural characteristics of ultrafine-grained nickel, *Mater. Sci. Eng. A* 391 (2005) 377-389.
15. P.V. Liddicoat, X.-Z. Liao, Y. Zhao, Y. Zhu, M.Y. Murashkin, E.J. Lavernia, R.Z. Valiev, S.P. Ringer, Nanostructural hierarchy increases the strength of aluminium alloys, *Nature Comm.* 1 (2010) 63.
16. R.Z. Valiev, D.A. Salimonenko, N.K. Tsenev, P.B. Berbon, T.G. Langdon, Observations of high strain rate superplasticity in commercial aluminum alloys with ultrafine grain sizes, *Scripta Mater.* 37 (1997) 1945.
17. C. Xu, M. Furukawa, Z. Horita, T.G. Langdon, Using ECAP to achieve grain refinement, precipitate fragmentation and high strain rate superplasticity in a spray-cast aluminum alloy, *Acta Mater.* 51 (2003) 6139-6149.
18. C. Xu, M. Furukawa, Z. Horita, T.G. Langdon, Severe plastic deformation as a processing tool for developing superplastic metals, *J. Alloys Compds.* 378 (2004) 27.
19. R.Z. Valiev, N.A. Enikeev, M. Yu. Murashkin, V.U. Kazykhanov, X. Sauvage, On the origin of the extremely high strength of ultrafine-grained Al alloys produced by severe plastic deformation, *Scripta Mater.* 63 (2010) 949-952.
20. G. Sha, K. Tugcu, X.Z. Liao, P.W. Trimby, M.Y. Murashkin, R.Z. Valiev, S.P. Ringer, Strength, grain refinement and solute nanostructures of an Al-Mg-Si alloy (AA6060) processed by high-pressure torsion, *Acta Mater.* 63 (2014) 169-179.

21. X. Sauvage, N. Enikeev, R. Valiev, Y. Nasedkina, M. Murashkin, Atomic-scale analysis of the segregation and precipitation mechanisms in a severely deformed Al-Mg alloy, *Acta Mater.* 72 (2014) 125-136.
22. K. Tugcu, G. Sha, X.Z. Liao, P. Trimby, J.H. Xia, M.Y. Murashkin, Y. Xie, R.Z. Valiev, S.P. Ringer, Enhanced grain refinement of an Al-Mg-Si alloy by high-pressure torsion processing at 100°C, *Mater. Sci. Eng. A* 552 (2012) 415-418.
23. M. Murayama, Z. Horita, K. Hono, Microstructure of two-phase Al-1.7 at% Cu alloy deformed by equal-channel angular pressing, *Acta Mater.* 49 (2001) 21.
24. C. Xu, M. Furukawa, Z. Horita, T.G. Langdon, Influence of ECAP on precipitate distributions in a spray-cast aluminum alloy, *Acta Mater.* 53 (2005) 749.
25. C.M. Cepeda-Jiménez, J.M. García-Infanta, O.A. Ruano, F. Carreño, High strain rate superplasticity at intermediate temperatures of the Al 7075 alloy severely processed by equal channel angular pressing, *J. Alloys Compd.* 509 (2011) 9589-9597.
26. C.M. Cepeda-Jiménez, C.M. Cepeda-Jiménez, J.M. García-Infanta, O.A. Ruano, F. Carreño, Achieving microstructures prone to superplastic deformation in an Al-Zn-Mg-Cu alloy by equal channel angular pressing, *J. Alloys Compd.* 546 (2013) 253-259.
27. P.J. Apps, M. Berta, P.B. Prangnell, *Acta Mater.* 53 (2005) 499-511.
28. A.P. Zhilyaev, J.M. García-Infanta, F. Carreño, T.G. Langdon, O.A. Ruano, *Scripta Mater.* 57 (2007) 763-765.
29. T. Pettersen, E. Nes, On the origin of strain softening during deformation of aluminum in torsion to large strains, *Metall. Mater. Trans. A* 34 (2003) 2727-2736.
30. A. Gholinia, P. Bate, P.B. Prangnell, Modelling texture development during equal channel angular extrusion of aluminium, *Acta Mater.* 50 (2002) 2121-2136.
31. G.R. Canova, U.F. Kocks, J.J. Jonas, Theory of torsion texture development, *Acta Metall.* 32 (1984) 211-226.

32. E.A. Korznikova, S.Yu.Mironov, A.V.Korznikov, A.P.Zhilyaev, T.G.Langdon, Microstructural evolution and electro-resistivity in HPT nickel, *Mater. Sci. Eng. A* 556 (2012) 437-445.
33. C. Xu, Z. Horita, T.G. Langdon, The evolution of homogeneity in an aluminum alloy processed using high-pressure torsion, *Acta Mater.* 56 (2008) 5168–5176.
34. O. Andreau, J. Gubicza, N.X. Zhang, Y. Huang, P. Jenei, T.G. Langdon, Effect of short-term annealing on the microstructures and flow properties of an Al–1% Mg alloy processed by high-pressure torsion, *Mater. Sci. Eng. A* 615 (2014) 231–239.
35. G. Nurislamova, X. Sauvage, M. Murashkin, R. Islamgaliev, R. Valiev, Nanostructure and related mechanical properties of an Al-Mg-Si alloy processed by severe plastic deformation, *Philos. Mag. Lett.* 88 (2008) 459-466.
36. G. Sha, Y.B. Wang, X.Z. Liao, Z.C. Duan, S.P. Ringer, T.G. Langdon, Influence of equal-channel angular pressing on precipitation in an Al–Zn–Mg–Cu alloy, *Acta Mater.* 57 (2009) 3123.
37. G. Sha, L. Yao, X. Liao, S.P. Ringer, Z.C. Duan, T.G. Langdon, Segregation of solute elements at grain boundaries in an ultrafine grained Al-Zn-Mg-Cu alloy, *Ultramicroscopy* 111 (2011) 500-505.
38. Y.H. Zhao, X.Z. Liao, Z. Jin, R.Z. Valiev, Y.T. Zhu, Microstructures and mechanical properties of ultrafine grained 7075 Al alloy processed by ECAP and their evolutions during annealing, *Acta Mater.* 52 (2004) 4589-4599.
39. F. Li, D. H. Bae, and A.K. Ghosh, Grain elongation and anisotropic grain growth during superplastic deformation in an AlMgMnCu alloy, *Acta Mater.* 45 (9) (1997) 3887-95.

40. K. Oh-ishi, Y. Hasi, A. Sadakata, K. Kaneko, Z. Horita, T.G. Langdon, Microstructural control of an Al-Mg-Si alloy using equal-channel angular pressing, *Mater. Sci. Forum* 396-402 (2002) 333-338.
41. B.B. Straumal, B. Baretzky; A.A. Mazilkin, F. Phillipp, O.A. Kogtenkova, M.N. Volkov, R.Z. Valiev, Formation of nanograined structure and decomposition of supersaturated solid solution during high pressure torsion of Al-Zn and Al-Mg alloys, *Acta Mater.* 52 (2006) 4469-4478.
42. B.B. Straumal, X. Sauvage, B. Baretzky, A.A. Mazilkin, R.Z. Valiev, Grain boundary films in Al-Zn alloys after high pressure torsion, *Scripta Mater.* 70 (2014) 59-62.
43. N.Q. Chinh, R.Z. Valiev, X. Sauvage, G. Varga, K. Havancsák, M. Kawasaki, B.B. Straumal, T.G. Langdon, Grain Boundary Phenomena in an Ultrafine-Grained Al-Zn Alloy with Improved Mechanical Behavior for Micro-Devices, *Adv. Eng. Mater.* 16 (2014) 1000-1009.

Figure 1. EBSD IPF maps in the ND and (111) pole figures corresponding to (a) the as-cast and (b) the T6 peak-aged condition of the AA6082 alloy before HPT processing; (c) The corresponding misorientation distribution histograms.

Figure 2. (a, b) Bright field TEM micrographs corresponding to the as-cast condition, before HPT deformation, showing a colony of  $\beta$ -phase particles. The selected area electron diffraction (SAED) pattern of the Al matrix (zone axis [011]) is shown in the insert of (a); (c) STEM HAADF micrograph showing  $\beta$  stable precipitates; (d,e) The corresponding elemental maps of (d) Mg and (e) Si.

Figure 3. (a) Bright field TEM micrograph corresponding to the T6 peak-aged condition before HPT deformation showing  $\beta''$  and  $\beta'$  nanoprecipitates. The SAED pattern of the Al matrix (zone axis [011]) is shown in the insert; (b) STEM HAADF micrograph; (d,e) The corresponding elemental maps of (d) Mg and (e) Si.

Figure 4. EBSD IPF maps in the ND acquired at the disk center regions of the (a) as-cast and (b) T6 peak-aged AA6082 alloy processed by HPT using 0.5 revolutions at RT; (c) The corresponding misorientation distribution histograms.

Figure 5. EBSD IPF maps in the ND and (111) pole figures acquired at the disk center regions of (a) the as-cast and (b) the T6 peak-aged AA6082 alloy processed by HPT using 5 revolutions at RT; (c) main simple shear texture components on the {111} pole figure; (d) The corresponding misorientation distribution histograms; (e) Histogram of linear intercepts measured in the EBSD maps of Figs. 5a and 5b using only high-angle boundaries (HABs,  $\theta > 15^\circ$ ).

Figure 6. EBSD IPF maps in the ND and (111) pole figures acquired at the disk edge regions of (a) the as-cast and (b) the T6 peak-aged AA6082 alloy processed by HPT using 5 revolutions at RT; (c) The corresponding misorientation distribution histograms;

(d) Histogram of linear intercepts measured in the EBSD maps of Figs. 5a and 5b using only high-angle boundaries (HABs,  $\theta > 15^\circ$ ).

Figure 7. (a) Bright field TEM micrograph and the corresponding SAED pattern illustrating the microstructure of the as-cast AA6082 alloy subjected to HPT processing (N=5; disk edge); (b, c) STEM HAADF micrographs showing pinning of GBs and triple junctions by  $\beta$  precipitates after HPT processing (red arrows); The corresponding Mg (d) and Si (e) elemental maps.

Figure 8. (a) Bright field TEM micrograph illustrating the microstructure of the T6 peak aged AA6082 alloy subjected to HPT processing (N=5; disk edge); (b, c) STEM HAADF micrographs illustrating the absence of precipitates; The corresponding Mg (d) and Si (e) elemental maps, both showing an homogenous distribution of alloying elements.

Figure 9. Vickers microhardness vs. distance across the diameter of the (a) as-cast and (b) T6 peak-aged HPT disks processed using different number of turns. The HV value for the unprocessed samples is indicated by a dashed line; (c) Vickers microhardness values plotted against the equivalent shear strain ( $\gamma$ ) for the two considered initial conditions.

Figure 10. True stress-true strain curves corresponding to the (a) as-cast and (b) T6 peak aged samples tested in tension at RT and at an initial strain rate of  $10^{-3} \text{ s}^{-1}$ , before and after HPT processing. The schematic drawing of the tensile sample and its location in the HPT disk is shown in the insert of (b).

Figure 11. True stress-true strain curves corresponding to the (a) as-cast and (b) T6 peak aged samples tested in tension at  $250^\circ\text{C}$  and at an initial strain rate of  $10^{-3} \text{ s}^{-1}$ , before and after HPT processing.

Figure 12. EBSD IPF maps in the normal to the gage length surface and (111) pole figures corresponding to the gauge length of the (a) as-cast and (b) T6 peak-aged materials, processed by HPT (N=5) and then tensile tested at 250°C and at an initial strain rate of  $10^{-3} \text{ s}^{-1}$ ; (c) Misorientation distribution histogram; (d and e) Histograms of horizontal and vertical linear intercepts measured in the corresponding EBSD maps of the (d) as-cast and (e) T6 peak-aged conditions.  $d_l$  and  $d_t$  are, respectively, the average grain size values measured along the longitudinal direction (parallel to the tensile axis) and the transverse direction (perpendicular to the tensile axis).

Accepted manuscript

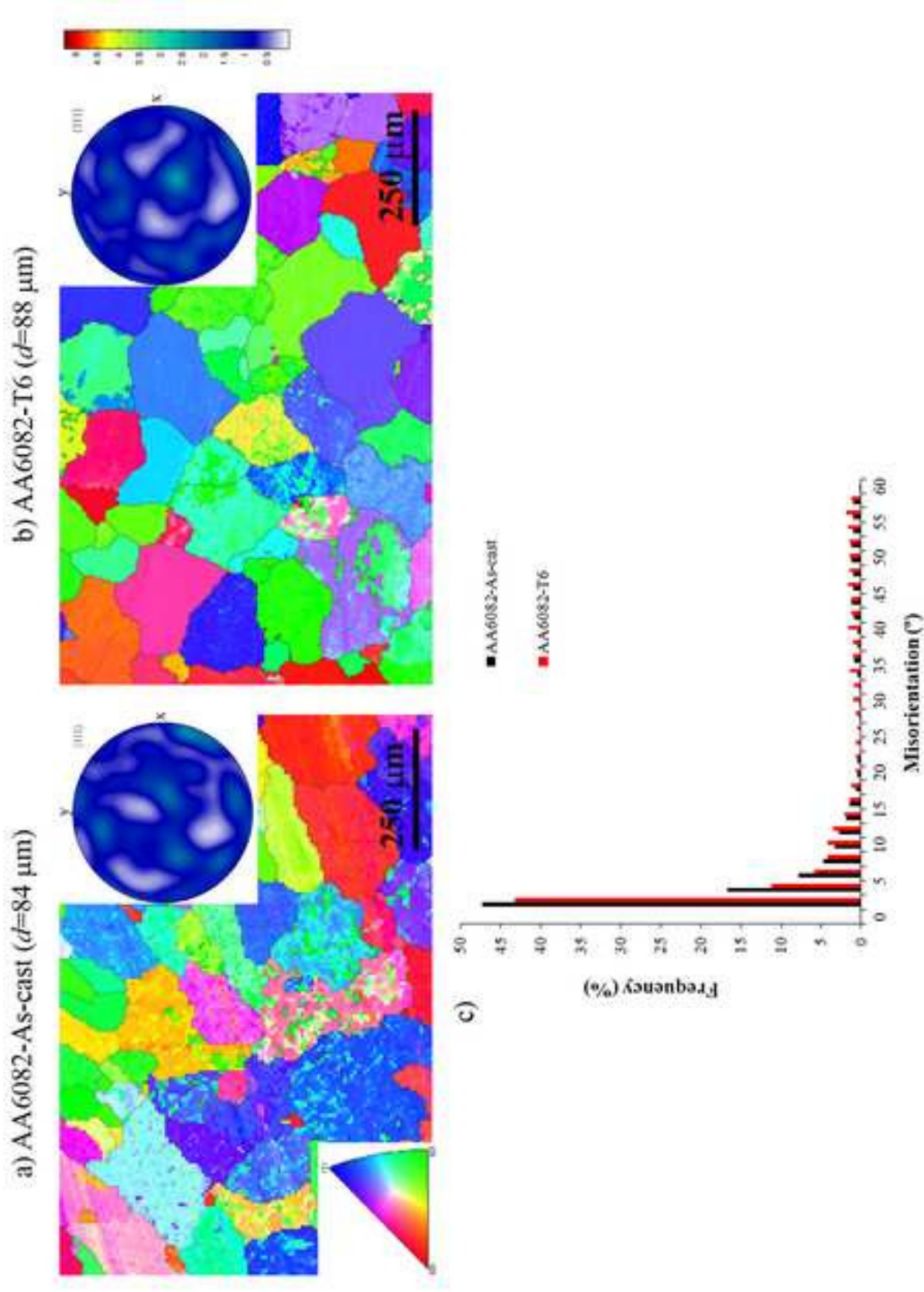


Figure 1. EBSD IPF maps in the ND and (111) pole figures corresponding to (a) the as-cast and (b) the T6 peak-aged condition of the AA6082 alloy before HPT processing; (c) The corresponding misorientation distribution histograms.

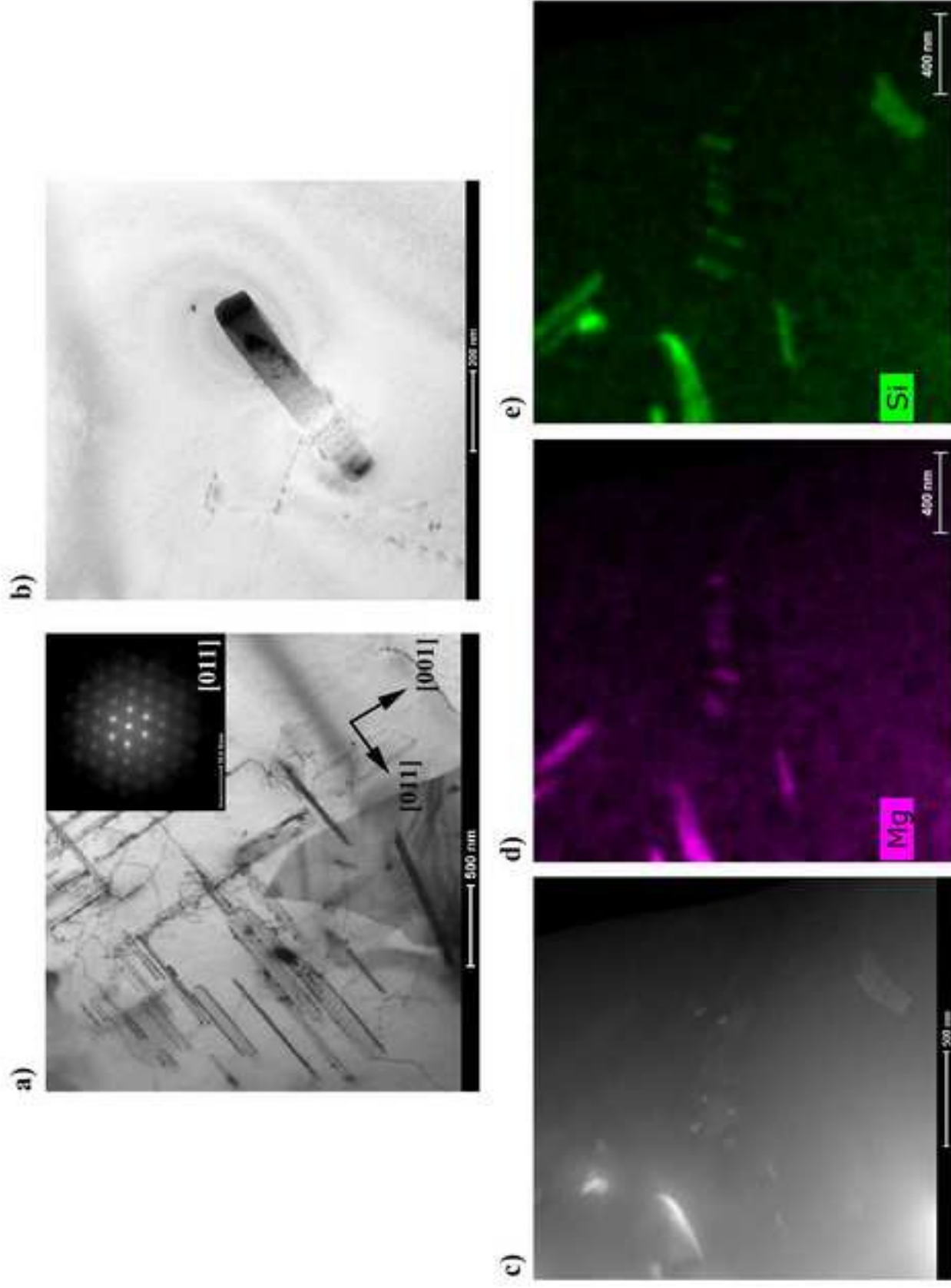


Figure 2. (a, b) Bright field TEM micrographs corresponding to the as-cast condition, before HPT deformation, showing a colony of  $\beta$ -phase particles. The selected area electron diffraction (SAED) pattern of the Al matrix (zone axis [011]) is shown in the insert of (a); (c) STEM HAADF micrograph showing  $\beta$  stable precipitates; (d,e) The corresponding elemental maps of (d) Mg and (e) Si.

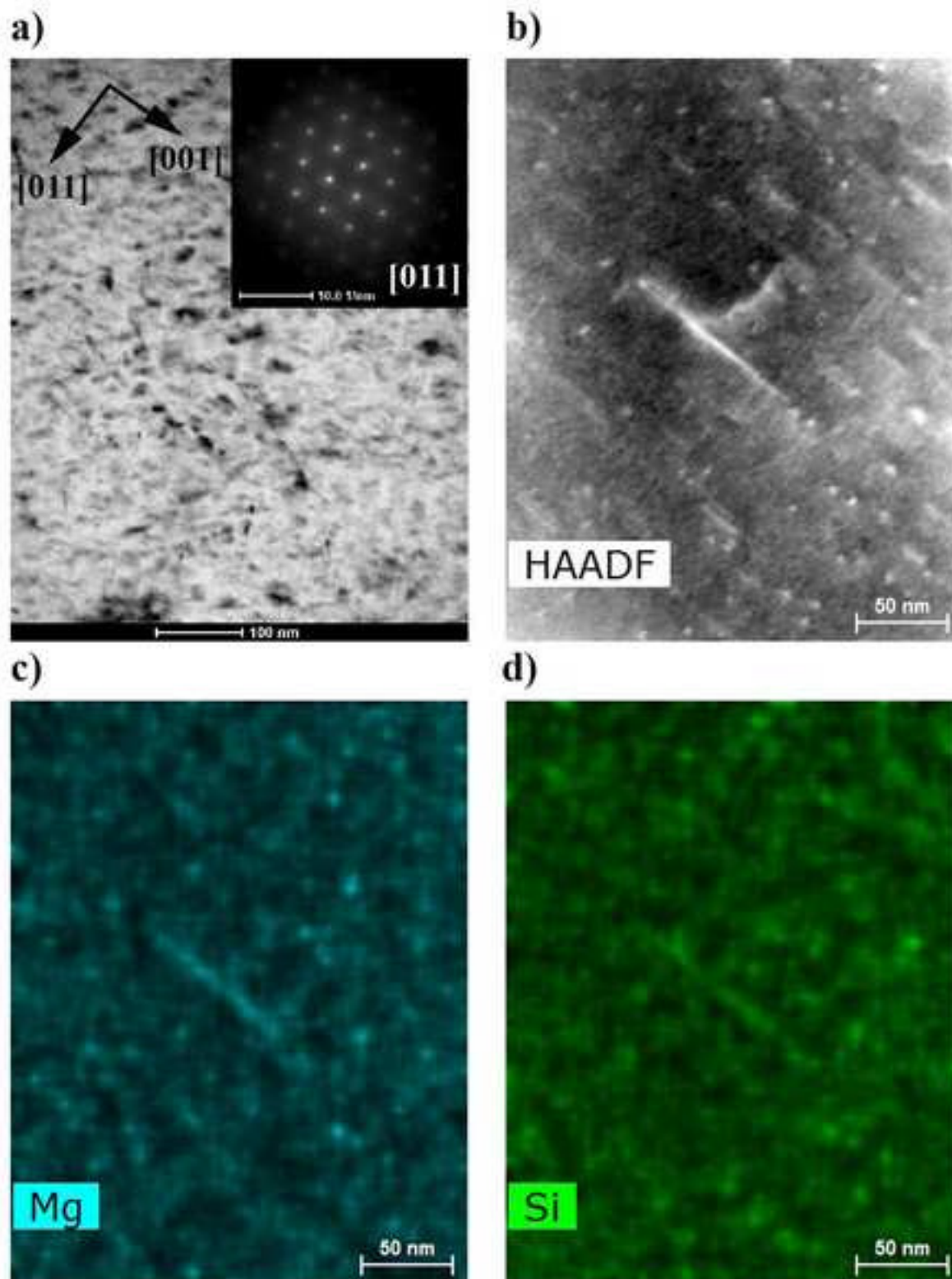


Figure 3. (a) Bright field TEM micrograph corresponding to the T6 peak-aged condition before HPT deformation showing  $\beta''$  and  $\beta'$  nanoprecipitates. The SAED pattern of the Al matrix (zone axis [011]) is shown in the insert; (b) STEM HAADF micrograph; (d,e) The corresponding elemental maps of (d) Mg and (e) Si .

a) AA6082-As-cast + HPT-N=0.5-Disk center ( $\gamma=0.63$ ) b) AA6082-T6 + HPT-N=0.5-Disk center ( $\gamma=0.63$ )

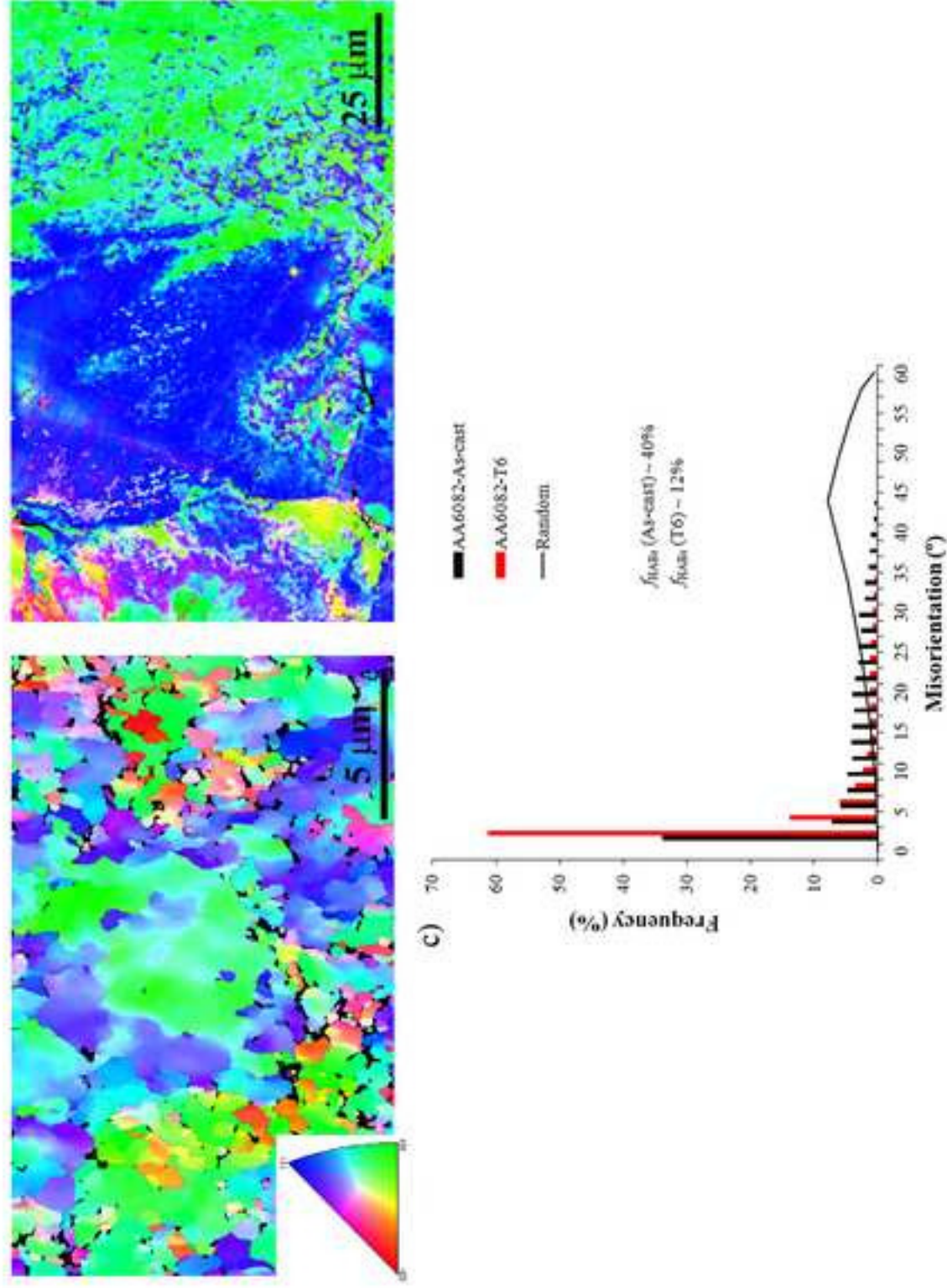


Figure 4. EBSD IPF maps in the ND acquired at the disk center regions of the (a) as-cast and (b) T6 peak-aged AA6082 alloy processed by HPT using 0.5 revolutions at RT; (c) The corresponding misorientation distribution histograms.

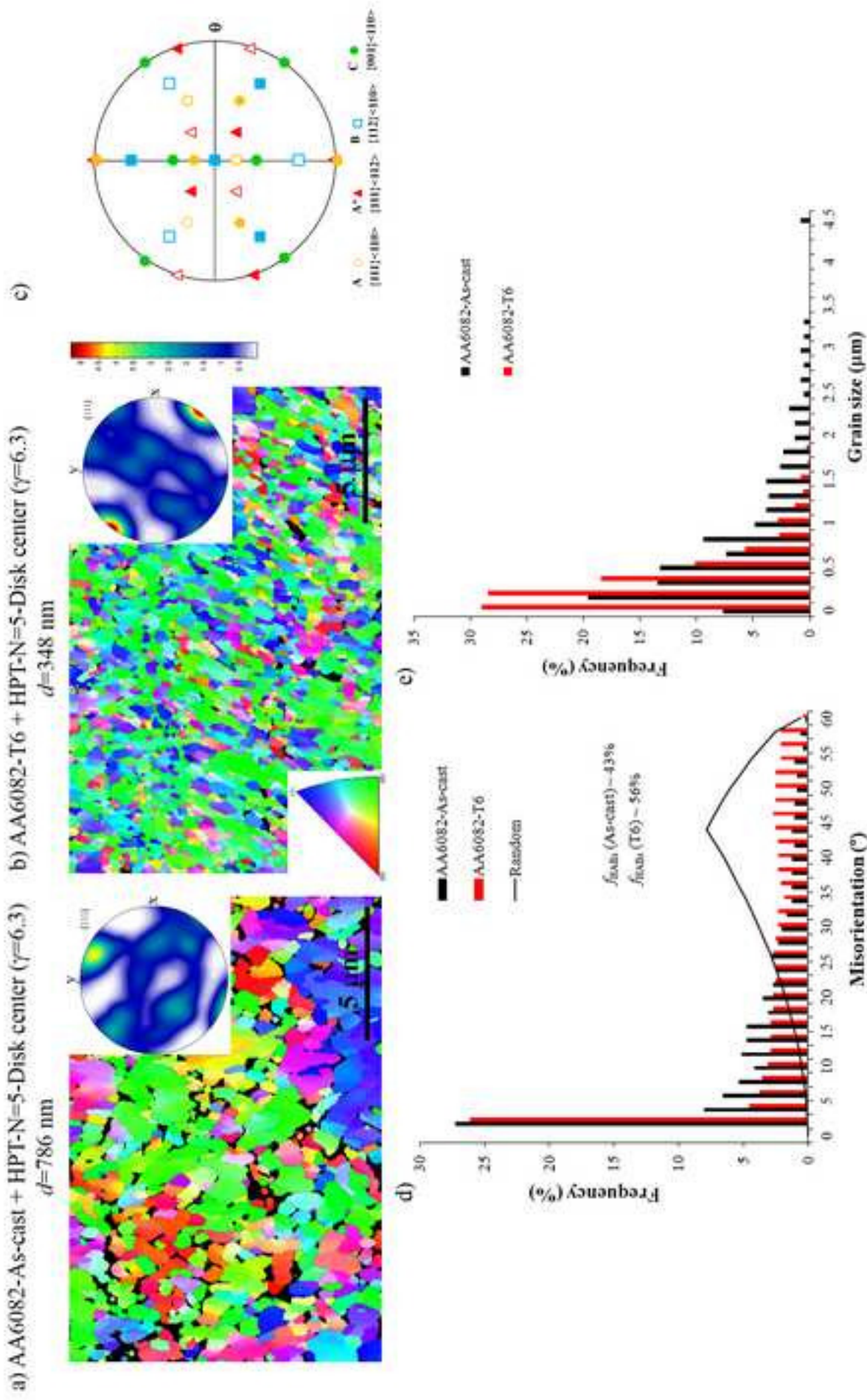


Figure 5. EBSD IPF maps in the ND and (111) pole figures acquired at the disk center regions of (a) the as-cast and (b) the T6 peak-aged AA6082 alloy processed by HPT using 5 revolutions at RT; (c) main simple shear texture components on the {111} pole figure; (d) The corresponding misorientation distribution histograms; (e) Histogram of linear intercepts measured in the EBSD maps of Figs. 5a and 5b using only high-angle boundaries (HABs,  $\theta > 15^\circ$ ).

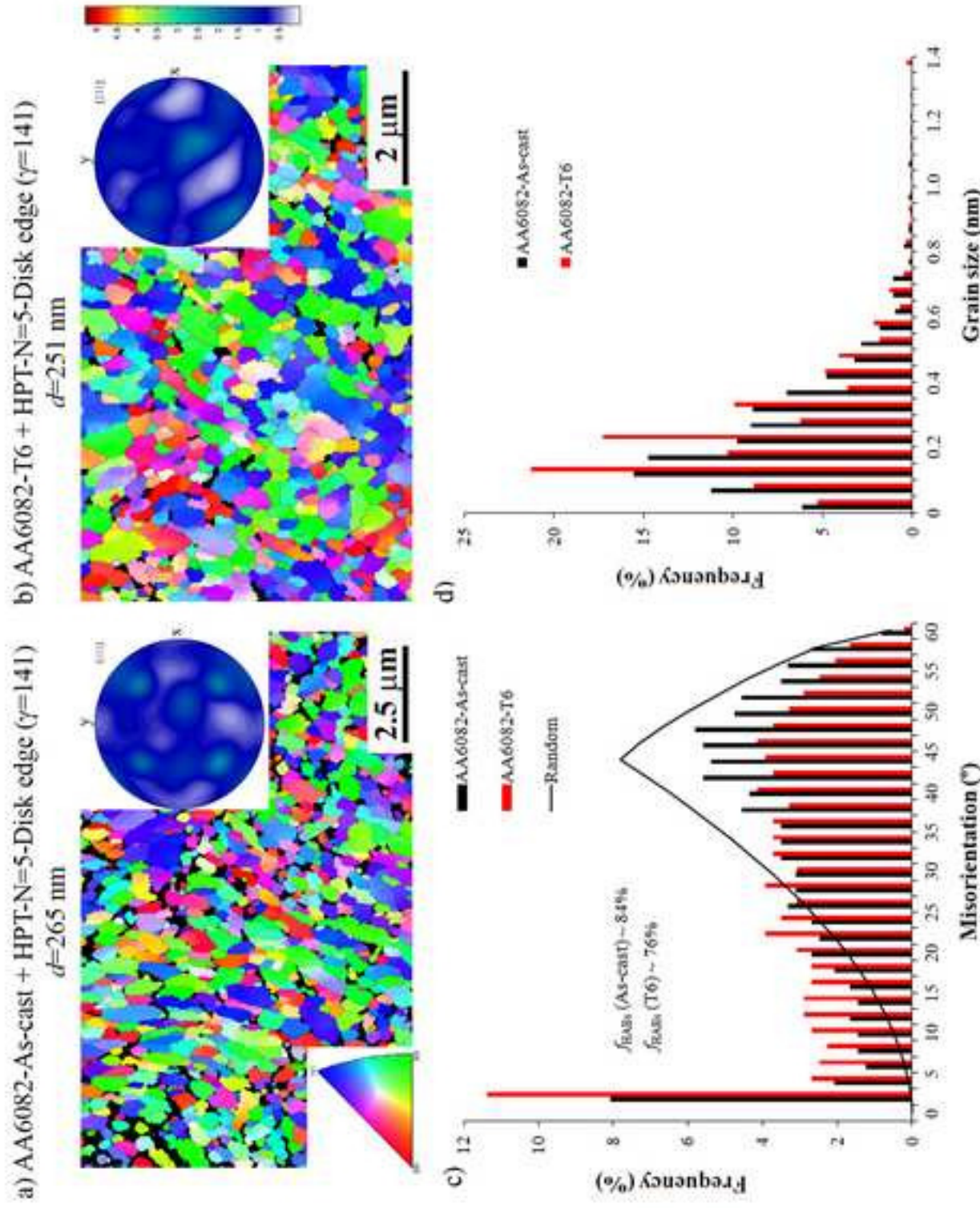


Figure 6. EBSD IPF maps in the ND and (111) pole figures acquired at the disk edge regions of (a) the as-cast and (b) the T6 peak-aged AA6082 alloy processed by HPT using 5 revolutions at RT; (c) The corresponding misorientation distribution histograms; (d) Histogram of linear intercepts measured in the EBSD maps of Figs. 5a and 5b using only high-angle boundaries (HABs,  $\theta > 15^\circ$ ).

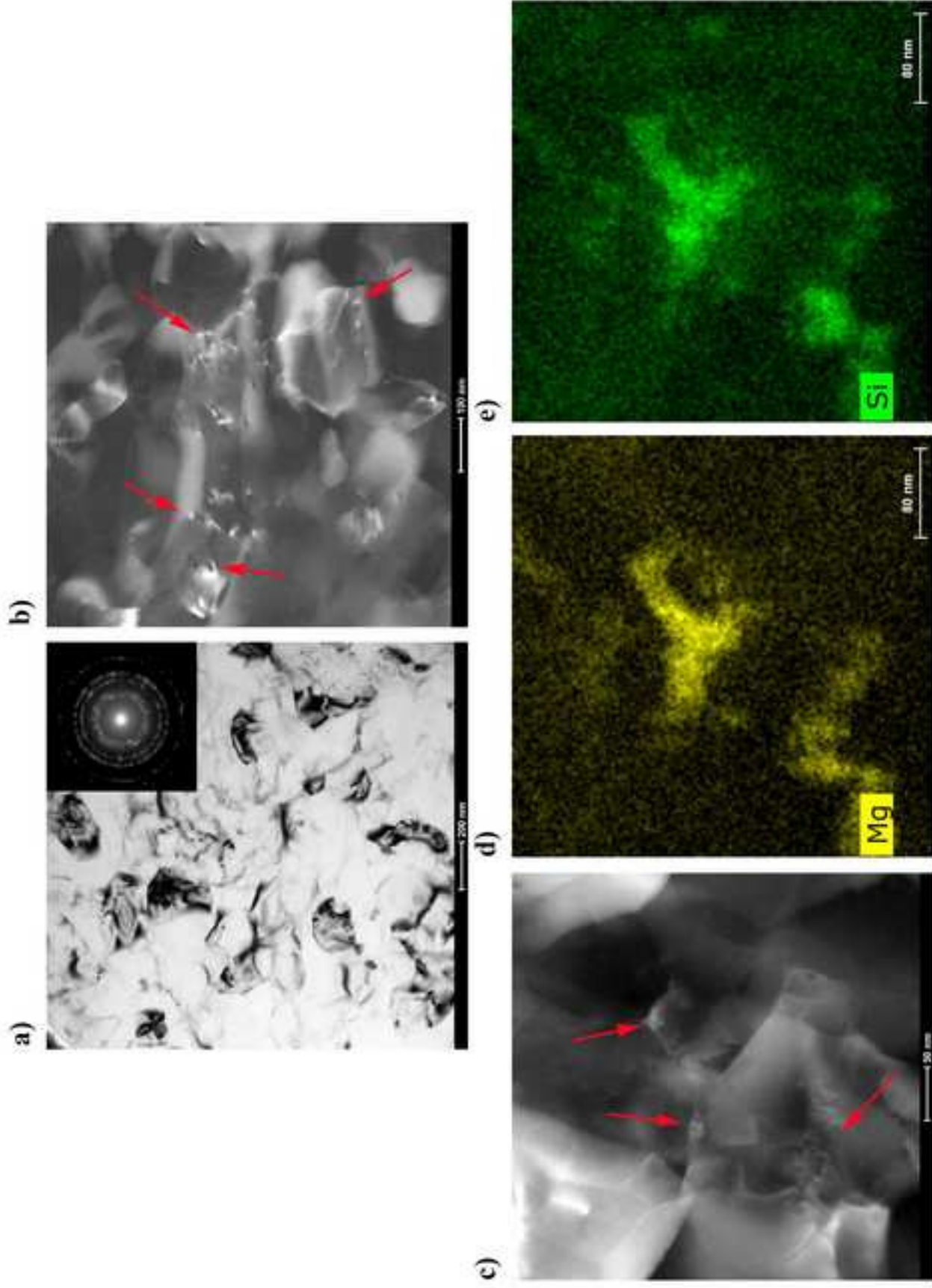


Figure 7. (a) Bright field TEM micrograph and the corresponding SAED pattern illustrating the microstructure of the as-cast AA6082 alloy subjected to HPT processing (N=5; disk edge); (b, c) STEM HAADF micrographs showing pinning of GBs and triple junctions by  $\beta$  precipitates after HPT processing (red arrows); The corresponding Mg (d) and Si (e) elemental maps.

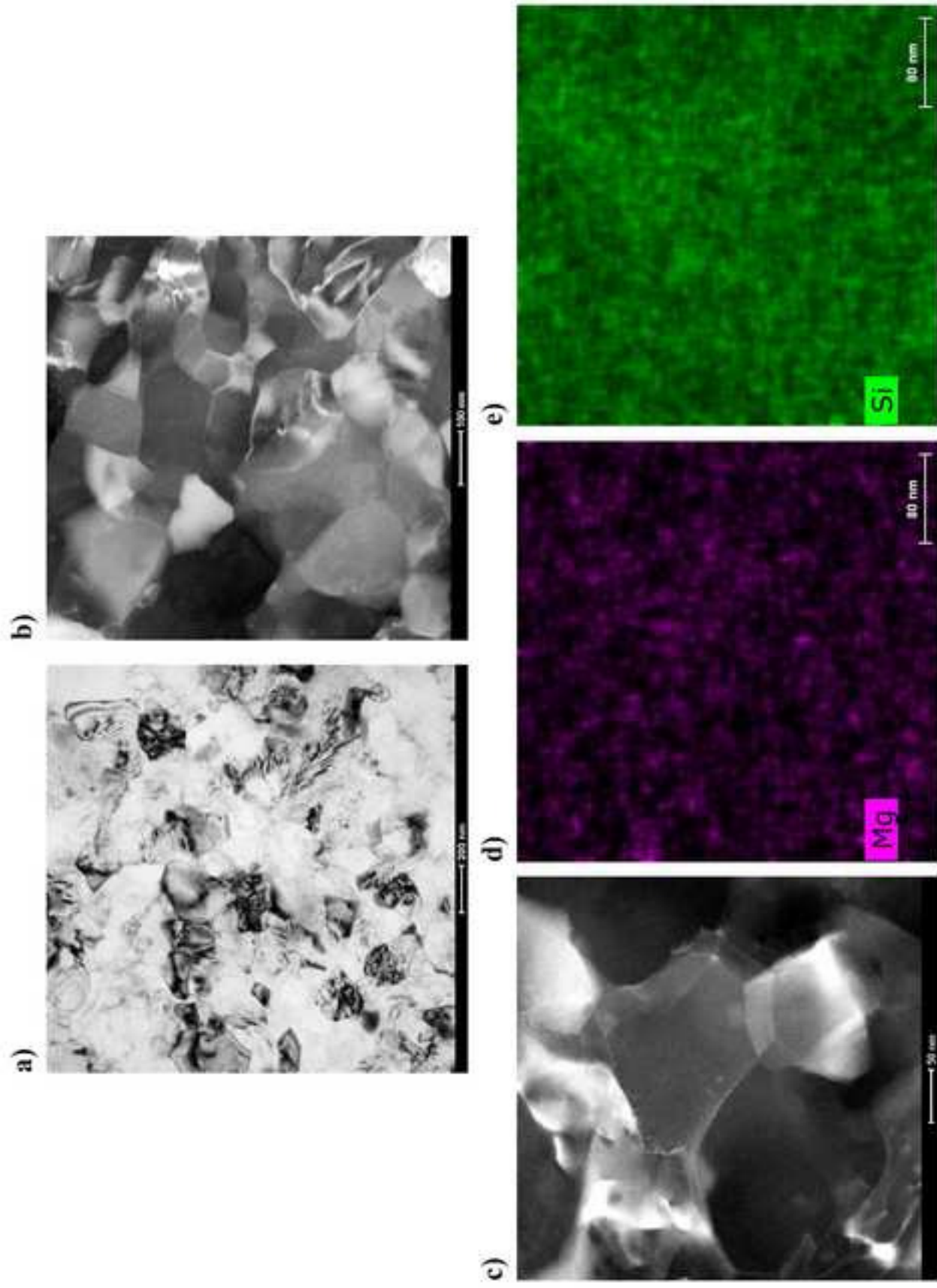


Figure 8. (a) Bright field TEM micrograph illustrating the microstructure of the T6 peak aged AA6082 alloy subjected to HPT processing (N=5; disk edge); (b, c) STEM HAADF micrographs illustrating the absence of precipitates. The corresponding Mg (d) and Si (e) elemental maps, both showing a homogenous distribution of alloying elements.

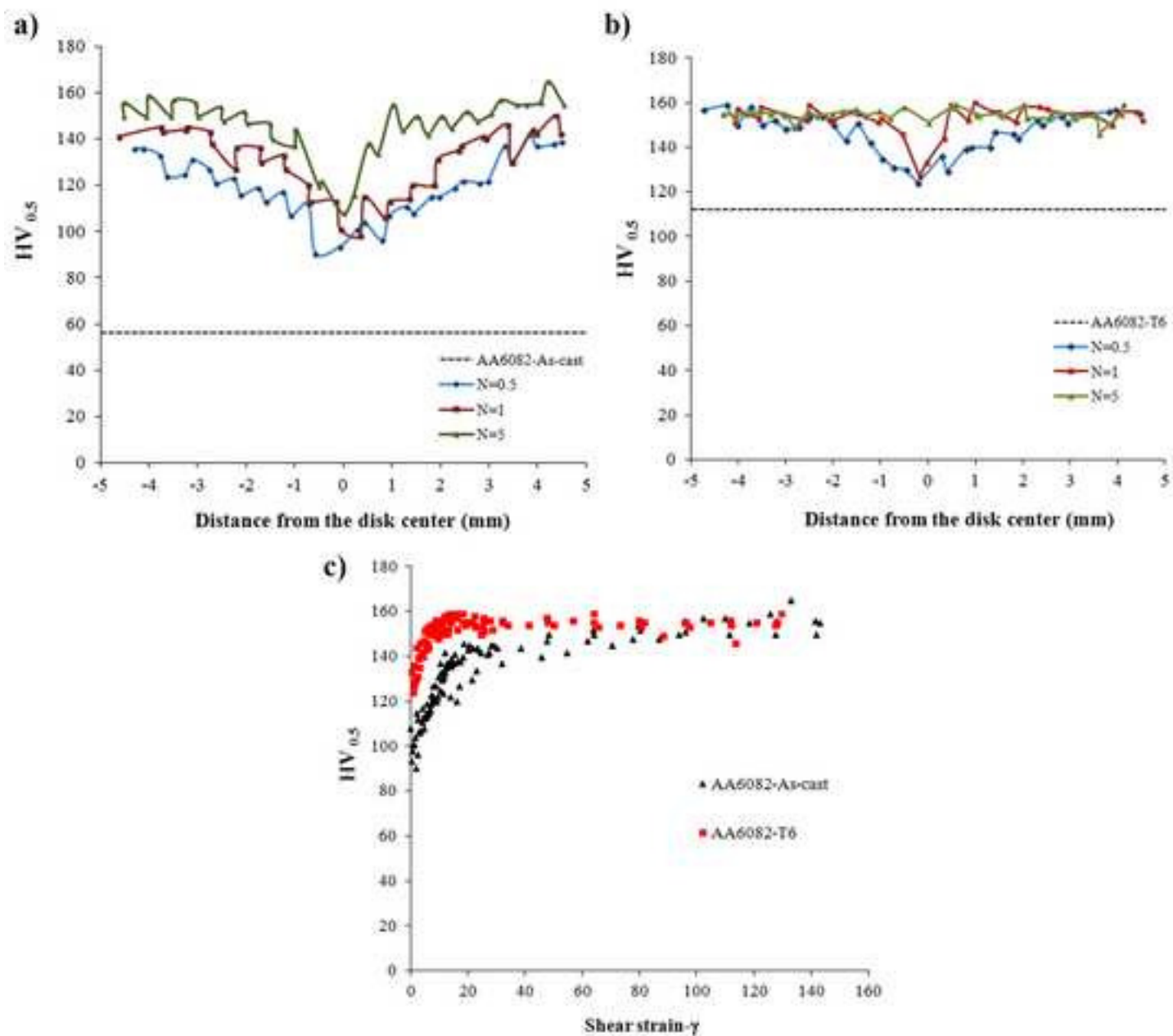


Figure 9. Vickers microhardness vs. distance across the diameter of the (a) as-cast and (b) T6 peak-aged HPT disks processed using different number of turns. The HV value for the unprocessed samples is indicated by a dashed line; (c) Vickers microhardness values plotted against the equivalent shear strain ( $\gamma$ ) for the two considered initial conditions.

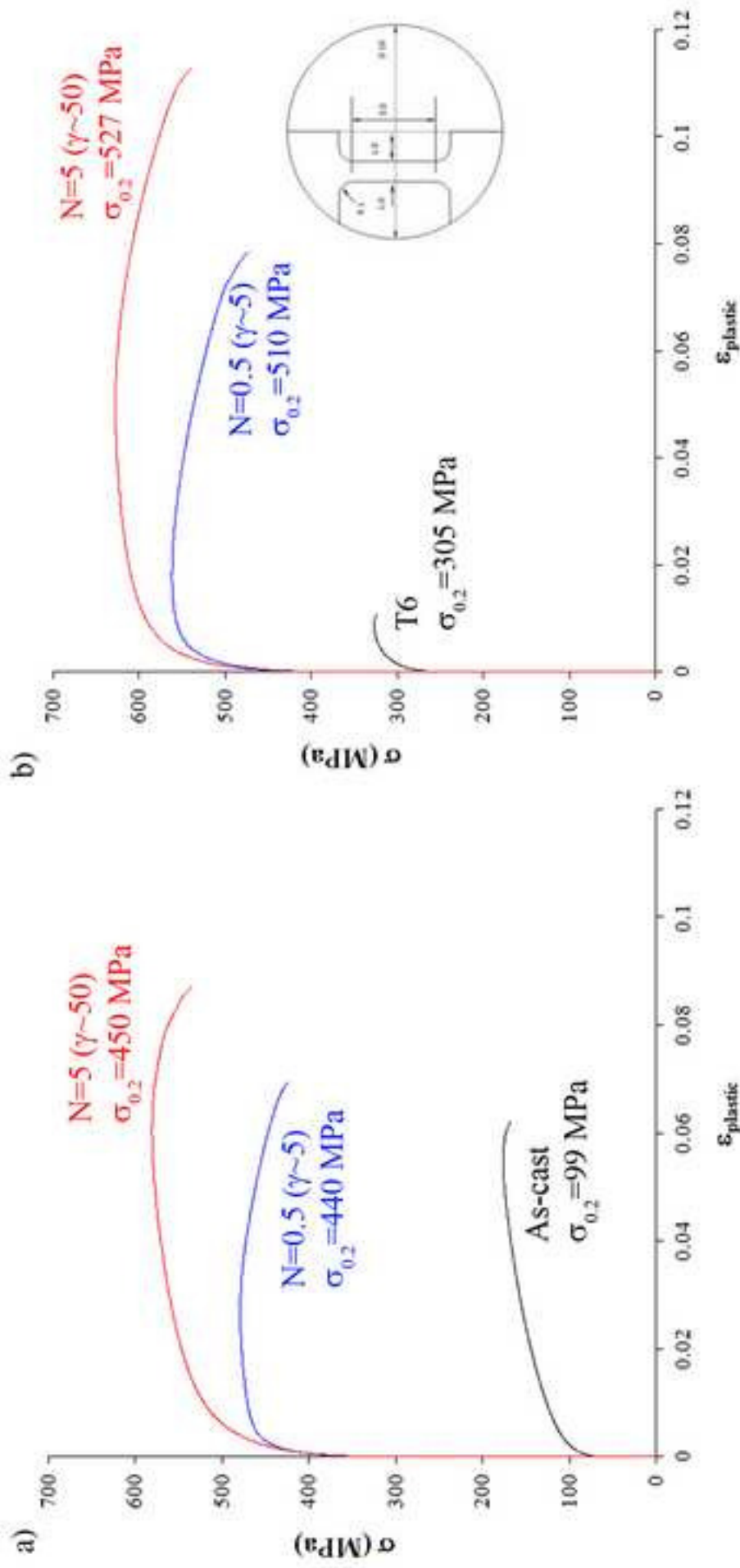


Figure 10. True stress-true strain curves corresponding to the (a) as-cast and (b) T6 peak aged samples tested in tension at RT and at an initial strain rate of 10<sup>-3</sup> s<sup>-1</sup>, before and after HPT processing. The schematic drawing of the tensile sample and its location in the HPT disk is shown in the insert of (b).

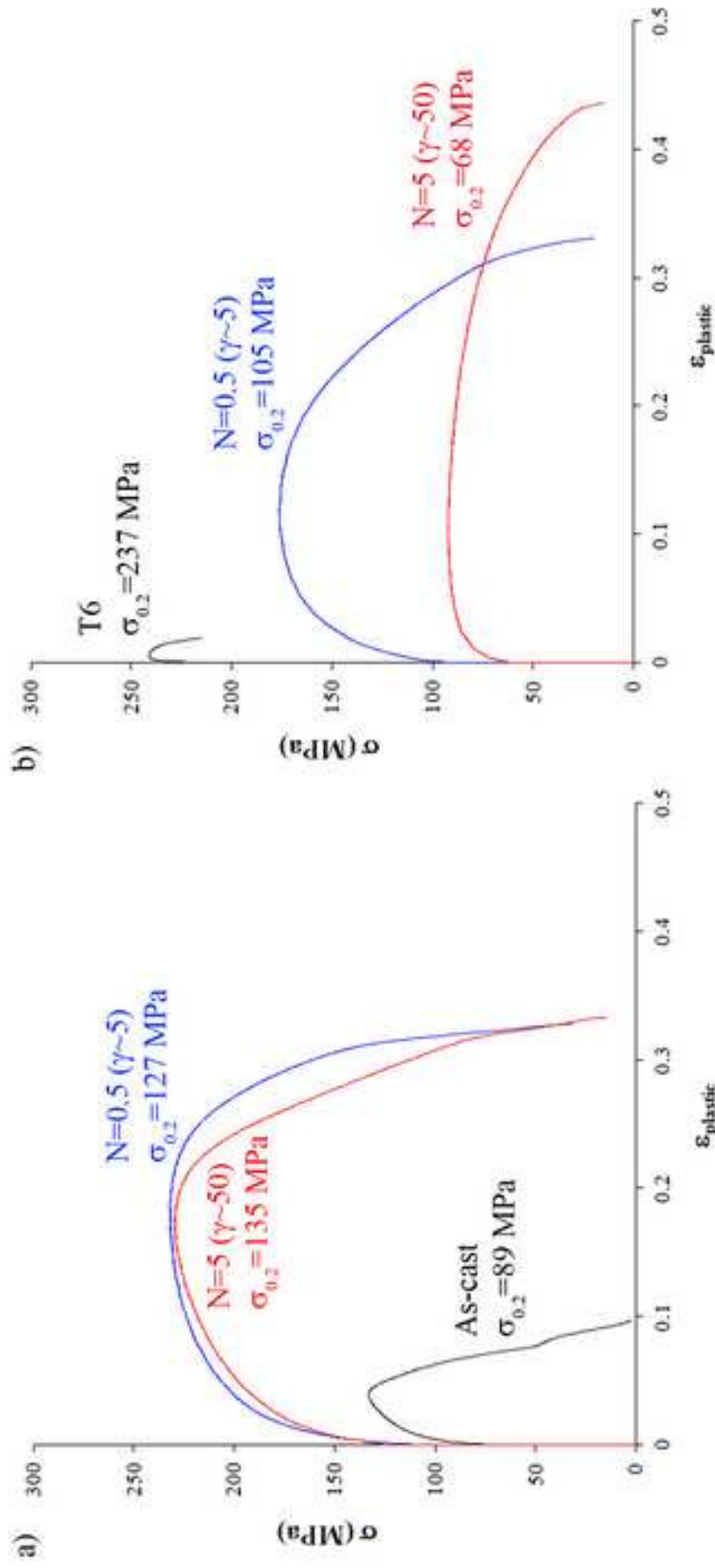


Figure 11. True stress-true strain curves corresponding to the (a) as-cast and (b) T6 peak aged samples tested in tension at 250°C and at an initial strain rate of 10<sup>-3</sup> s<sup>-1</sup>, before and after HPT processing.

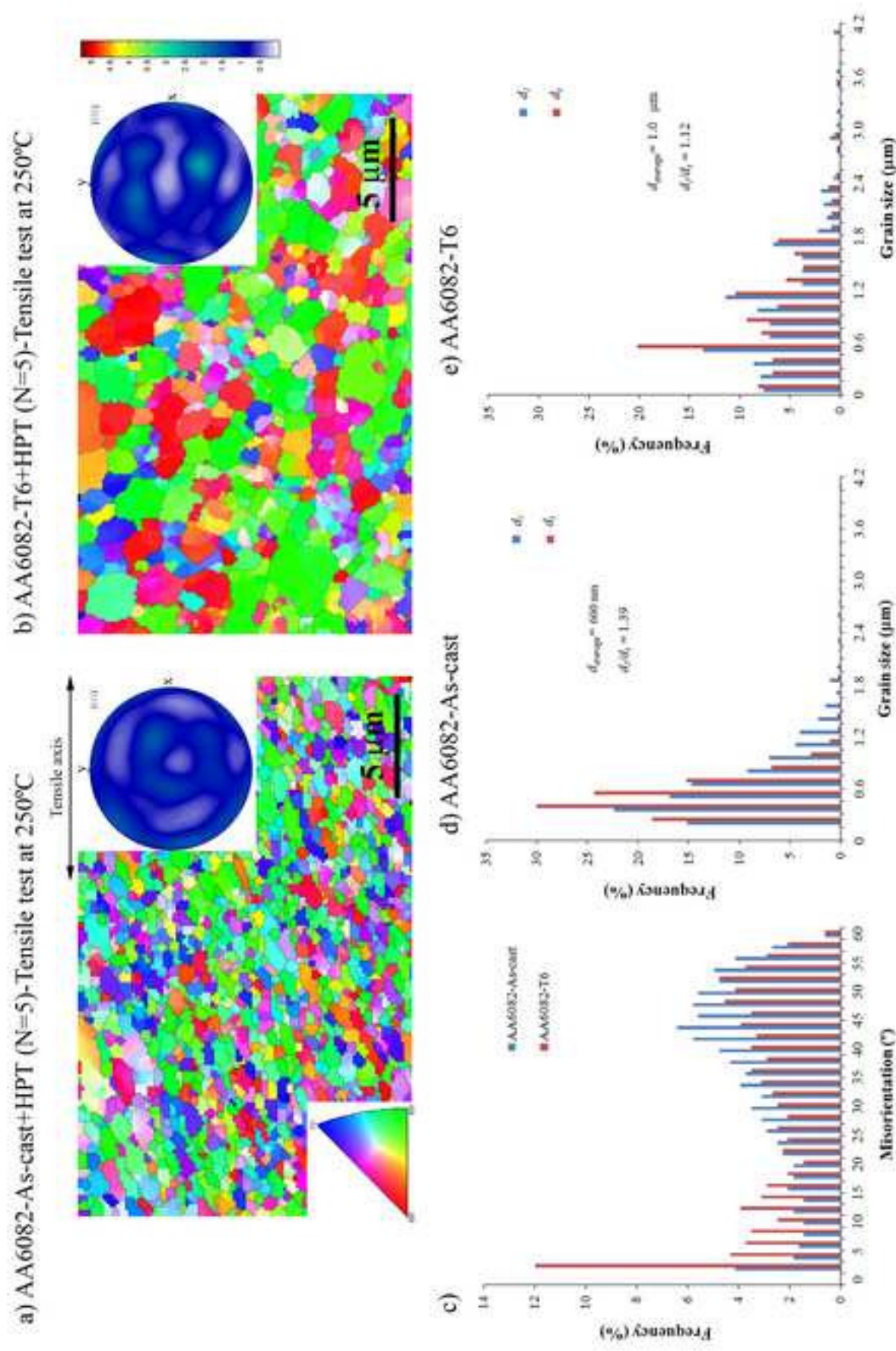


Figure 12. EBSD IPF maps in the normal to the gage length surface and (111) pole figures corresponding to the gauge length of the (a) as-cast and (b) T6 peak-aged materials, processed by HPT (N=5) and then tensile tested at 250°C and at an initial strain rate of 10<sup>-3</sup> s<sup>-1</sup>; (c) Misorientation distribution histogram; (d and e) Histograms of horizontal and vertical linear intercepts measured in the corresponding EBSD maps of the (d) as-cast and (e) T6 peak-aged conditions.  $d_1$  and  $d_2$  are, respectively, the average grain size values measured along the longitudinal direction (parallel to the tensile axis) and the transverse direction (perpendicular to the tensile axis).